



GEOSCIENCES

Spectral Linear Mixing Model application in passive microwave data to analyze Antarctic surface melting dynamics (1978-2018)

CLAUDIO W. MENDES JÚNIOR, JORGE ARIGONY NETO, FERNANDO L. HILLEBRAND, MARCOS W.D. DE FREITAS, JULIANA COSTI & JEFFERSON C. SIMÕES

Abstract: Several studies have utilized passive microwave imagery for monitoring snowmelt in Antarctica. However, due to the low spatial resolution of these images (25 km), the quantification of snowmelt is not precise. To enhance the accuracy of these estimations, this study proposed a subpixel analysis approach based on a Spectral Linear Mixing Model. This approach was applied to images obtained from channels 18/19 GHz and 37 GHz, both horizontally and vertically polarized, acquired from the Scanning Multichannel Microwave Radiometer (SMMR), Special Sensor Microwave Imager (SSM/I), and Special Sensor Microwave Imager/Sounder (SSM/IS) instruments, spanning the period 1978-2018. The spatiotemporal analysis of the estimated snowmelt fraction images indicated that the most persistent and intensive melt was observed on the Antarctic Peninsula, particularly on the Larsen, Wilkins, George VI, and Wordie ice shelves. The melting period in the Antarctic Peninsula began in late October, with a peak in early January, and ended in late March. Other regions with persistent and intensive snowmelt were Mary Bird Land and Wilkes Land, followed by Dronning Maud Land, Amery Ice Shelf, Filchner-Ronne Ice Shelf, and Ross Ice Shelf. These snowmelt data are valuable for modeling the impacts of snowmelt on glacial systems, local coastal environments, and sea-level rise.

Key words: Antarctica, Remote sensing, Passive microwave sensor, snowmelt, Spectral Linear Mixing Model.

INTRODUCTION

Monitoring surface glacier melting is highly relevant for investigating the impacts of climate warming in some regions of the Earth, especially for the smaller and more dynamic outlet glaciers of the Greenland ice sheet and the Antarctic coastal areas, which have experienced the most rapid changes due to atmospheric warming in these regions (Cook & Vaughan 2010, Bevan et al. 2020).

The occurrence of hot summers, a significant increase in the number of days with positive temperatures throughout the year, and longer

ablation conditions in the Antarctic Peninsula have caused significant changes in the glacier systems, especially in the last decades, such as glacier front retreat, the disintegration of ice shelves, reduction in seasonal sea ice coverage, and changes in local precipitation patterns. In this context, a large number of glaciers in this region have shown rapid variations in surface mass and energy balances, accumulation and ablation patterns, and glacier flow acceleration (Scambos et al. 2000, Torinesi et al. 2003, Cook & Vaughan 2010, Barrand et al. 2013, Trusel et al. 2012, Bevan et al. 2020).

Multi-temporal remote sensing images can be applied in the study of the dynamics of glacier surface melting areas in extensive and difficult-to-access areas that require high logistical costs, such as the Polar Regions. Images obtained by active and passive microwave sensors can be applied in the monitoring of these glaciers, even under low solar illumination and cloud cover conditions, which are very frequent in the Antarctic continent, and make it difficult to regularly obtain images by optical sensors.

Microwave radiation data from Earth's surface were recorded every other day from October 1978 to August 1987 by Scanning Multichannel Microwave Radiometer (SMMR), onboard the Nimbus 7 satellite, and recorded daily from July to May 2009 by Special Sensor Microwave-Imager (SSM/I), from the Defense Meteorological Satellite Program (DMSP). Data from SMMR and SSM/I on the DMSP F8, F10, F11, F13, and F14 satellites comprise a time series of brightness temperature (T_b) from Earth's surface from 1978 to 2009. This time series can be extended to the present, by using data acquired since 2005 from the Special Sensor Microwave Imager/Sounder (SSM/IS) on the DMSP F16 satellite. Images acquired from these sensors can be used to detect snowmelt and dry snow areas, based on the rapid increase of brightness temperature at the onset of snowmelt and a sharpening contrast of lower brightness temperature observed during nonmelt conditions (Liu et al. 2006).

Due to the low power of microwave radiation emitted by the Earth's surface, passive microwave sensors operate with a large Instantaneous Field of View (IFOV) to collect enough energy and produce a detectable signal, resulting in images with a very low spatial resolution (25 km). Because of this resolution, methods for analyzing snowmelt areas from these images did not result in precise estimations. To improve

the accuracy of these estimations, Mendes Jr. (2010) proposed a subpixel analysis approach for the analysis of snowmelt areas in the Antarctic Peninsula through SMMR and SSM/I images, using a Spectral Linear Mixing Model (SLMM). Data derived from this SLMM was used to quantify more accurately the evolution trend of the snowmelt areas in the Antarctic Peninsula from 1978 to 2008, and their persistence, intensity, duration, and spatiotemporal variability, during the austral summers of that period. To update this research, we proposed in this study the monitoring of snowmelt areas for a longer period (1978-2018), now comprising the whole Antarctic continent, through the application of the SLMM developed by Mendes Jr. (2010).

DETECTION OF SNOWMELT AREAS IN PASSIVE MICROWAVE IMAGES

Passive microwave sensors enable the discrimination between areas of superficial snowmelt and dry snow through their imagery. This is due to the higher emissivity of liquid water present in the snowpack. A passive microwave sensor detects the energy emitted by the snowpack within its IFOV. The snowpack density, temperature, crystal structure, and grain size contribute to the emissivity of the snowpack, but the most significant changes in brightness temperature occur when there are changes in the liquid water content. The primary effect of dry snow coverage at frequencies above 10 GHz is to scatter radiation inside the snowpack because snow particles have a size similar to the wavelength of this electromagnetic radiation (Abdalati & Steffen 1997).

Snowmelt areas have high absorption and reduced volumetric scattering due to the presence of liquid water. The surface scattering is increased by a factor of two over the volumetric scattering, resulting in a substantial increase

in snow emissivity. Therefore, the physical mechanism for detecting snowmelting areas is that the microwave emissivity of a snowpack dramatically increases in response to the introduction of a small amount of liquid water (Mote et al. 1993).

The passive microwave sensor images from SMMR, SSM/I, and SSM/IS sensors comprise a daily database of the surface brightness temperature of the Earth's surface since 1978. In several studies, the 19 GHz and 37 GHz channels of the SSM/I and SSM/IS sensors (and the corresponding 18 GHz and 37 GHz channels of the SMMR sensor), in both horizontal and vertical polarizations, have been used to detect snowmelt areas. The most suitable images for detecting snowpack melting conditions are captured by satellite sensors operating in specific orbits. These include the descending orbit of DMSP-F8 (SSM/I), the ascending orbits of Nimbus-7 (SMMR), and the other DMSP satellites (SSM/I and SSM/IS), because microwave

radiation emissions in daytime periods are more intense than at other times.

Figure 1 shows a sample of SSM/I F13 images of Antarctica (19H channel - ascending orbit), obtained during the austral winter and summer. In this figure, we can observe a large sea extension in the SSM/I image of the austral winter (a), along with high values of brightness temperatures in the SSM/I image of the austral summer (b), mainly in the coastal areas of the Antarctic continent, due to the snowmelting.

The electromagnetic radiation emitted by targets at the frequencies of 18 GHz, 19GHz, and 37GHz is not affected by atmospheric constituents (i.e., gases, water vapor, suspended particulate matter, and aerosols). Therefore, images from these frequencies are suitable for snowmelt monitoring using time-series data from passive microwave sensors without any atmospheric interference (Liu et al. 2006).

To use data from these different sensors, the brightness temperatures must be recalibrated. Based on overlapping observations of SMMR

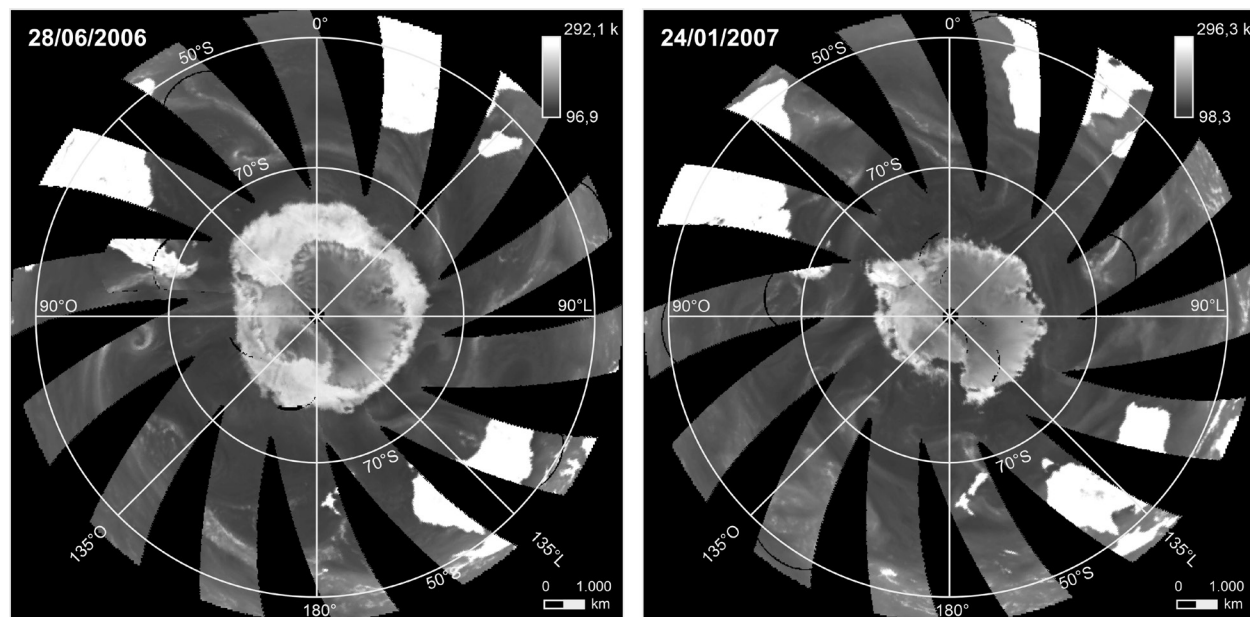


Figure 1. SSM/I F13 images of the southern hemisphere (spatial resolution of 25 km), covering the Antarctic continent and Austral Ocean (19H band - ascending orbit), acquired in austral winter (a) and summer (b), in the Lambert Azimuthal Equal-area projection (EASE-Grid format).

and SSM/I F8 sensors over Antarctica, Jezek et al. (1993) calculated linear regression equations to calibrate SSMR data. Abdalati et al. (1995) made comparisons of brightness temperatures from SSM/I instruments on the DMSP F8 and F11 satellites for Antarctica and the Greenland ice sheets. Freitas et al. (2018) estimated linear regression coefficients to calibrate SSM/IS F17 data using SSM/I F13 pre-calibrated data as a reference. Calibrated data by these regression coefficients, for channels 18 GHz of SSMR, 19 GHz of SSM/I and SSM/IS, and 37 GHz for all these sensors, were used in several studies to detect the extent, onset date, end date, and duration of snowmelt in Antarctica.

Zwally & Fiegles (1994) mapped the extent of the melting zone of the Antarctic continent during the period 1978-1987, through the classification of SSMR images. Ridley (1993), Fahnestock et al. (2002), and Torinesi et al. (2003) used SSMR and SSM/I data to detect surface melting on the Antarctic Peninsula ice margins during the periods 1978-1991, 1978-2000, 1980-1999, respectively. SSMR and SSM/I data were used by Comiso (2000) to investigate the variability and trends in Antarctic surface temperatures during 1979-1998. Liu et al. (2005) developed a wavelet transform-based edge detection approach to derive the snowmelt onset, end date, and duration in Antarctica. These authors used this approach to calculate the average annual melt extent, intensity, and duration for austral summers from 1978 to 2004 (Liu et al. 2006).

However, in all of these researches, passive microwave images were applied to detect snowmelt in the entire area of each pixel covering the Antarctic continent. Freitas et al. (2018) called these Boolean snowmelt detection approaches and observed that if they consider the total area of a pixel as snowmelt, they could overestimate this measurement. To improve

these Boolean methods, Mendes Jr. (2010) and Freitas et al. (2018) proposed a subpixel analysis of passive microwave images to get more accurate estimations of snowmelt areas.

SPECTRAL LINEAR MIXING MODEL

This research proposes the application of one approach widely used in the subpixel analysis of land cover types in remote sensing imagery, the so-called Spectral Linear Mixing Model (SLMM), developed by Adams et al. (1986), Shimabukuro (1987), and Shimabukuro & Smith (1991). According to these authors, the SLMM is based on the assumption that the spectral response of a pixel (in terms of digital number, radiance, or reflectance) is a linear combination of the spectral response of each component or target in the sensor's IFOV. In this case, the spectral response recorded by the sensor results from the atmospheric contribution and the average value of the spectral response of all targets (components) within its IFOV. The contribution of each component is weighted based on the spatial extent it occupies within the IFOV. Thus, each pixel of a given image, which can assume any value within the grayscale range, contains information about the spectral response and proportion of each component.

In the SLMM proposed by Mendes Jr. (2010) and Freitas et al. (2018), the spectral response or brightness temperature (k) of each pixel i in a given spectral band k ($R_{i,k}$) is a linear combination of the spectral signature of each pure component j (i.e., Snowmelt Area or SM, Dry Snow Area or DS, and Rock Outcrops) in band k ($r_{j,k}$), weighted by the proportional area (values from 0 to 1) of each component in a given pixel (fraction $F_{i,j}$):

$$R_{i,k} = (F_{i,SM} * r_{SM,k}) + (F_{i,DS} * r_{DS,k}) + (F_{i,rock} * r_{rock,k}) + E_k \quad (\text{Equation 1})$$

Equation 1 can also be expressed in matrix form: where E_k is the least squares estimation error.

$$R_k = (F * r_k) + E_k \quad (\text{Equation 2})$$

Being n the number of pixels and m the number of pure components, we have:

R_k = n -dimensional vector of the spectral response of the pixels in spectral band k ;

F = $n \times m$ matrix of proportions;

r_k = m -dimensional vector of the spectral response of the pure components in band k ;

E_k = the least squares estimation error.

The resulting system of equations is solved through the least squares fitting method, whose goal is to estimate the fraction of components F , minimizing the sum of the squared errors E_k , subject to the constraints that the fraction of a certain component's pixel is greater than or equal to zero, and that the sum of the fractions of the components in each pixel is equal to 1 (i.e., 100% of the area of that pixel) (Shimabukuro & Smith 1991).

For the application of this SLMM, in addition to the images of the four channels, it is necessary to indicate the brightness temperature value of the pure components or endmembers. The value of the spectral signature of each endmember in this mixture model is critical for the correct estimation of their proportions.

The biggest challenge in applying the SLMM is determining the spectral response of these endmembers, as it is rare to find a pixel that contains exclusively the response of a single component. This is even more difficult in passive microwave sensor images, as they have a very low spatial resolution (25 km). To estimate the spectral signatures of the pure components SM, DS, and rock outcrops in the Antarctic Peninsula, Mendes Jr. (2010) and Freitas et al. (2018) proposed the use of co-registered images from SSM/I F-13 and Advanced Synthetic Aperture

RADAR (ASAR - ENVISAT satellite), which were pre-processed and used in a SLMM for subpixel analysis of snowmelt areas in SSM/I images.

In these researches were used SSM/I sensor images obtained in the austral spring of 2006, autumn of 2007, and summers of 2006/2007 and 2007/2008 from 19 GHz and 37 GHz channels, in both horizontal and vertical polarizations. These data were radiometrically calibrated using regression equations calculated by Abdalati et al. (1995).

Freitas et al. (2018) applied this SLMM for melt detection in the Antarctic Peninsula (1999-2009). In that research, the calibrated SSM/I F13 data (19 and 37 GHz channels) were compared to the components' proportion (fraction images) of the study area endmembers (SM, DS, and Rocks), derived from classified ASAR images on wide swath mode - WS (75 m). These ASAR images were classified by decision rules proposed by Mendes Jr. (2010). Additional details about this method of detection and classification of snowmelt in ASAR images can be found in Mendes Jr. et al. (2022).

Figure 2 shows an example of a classified ASAR WS image and its respective calibrated SSM/I channels (24/01/2007), used in the SLMM to estimate the spectral signatures of endmembers (SM, DS, and Rocks). These images had to be resampled to a spatial resolution with multiple values (75,505 m for the ASAR image and 25,067.66 m for the SSM/I channels), so that an SSM/I pixel corresponded to a matrix of 332 x 332 co-registered pixels from the classified ASAR image. A moving window with these dimensions was applied to the ASAR images for the calculation and generation of a fraction image for each endmember, with the same spatial resolution as the four SSM/I channels.

The fraction image of each pure component (derived from the classified ASAR image) and the four calibrated SSM/I channels (both

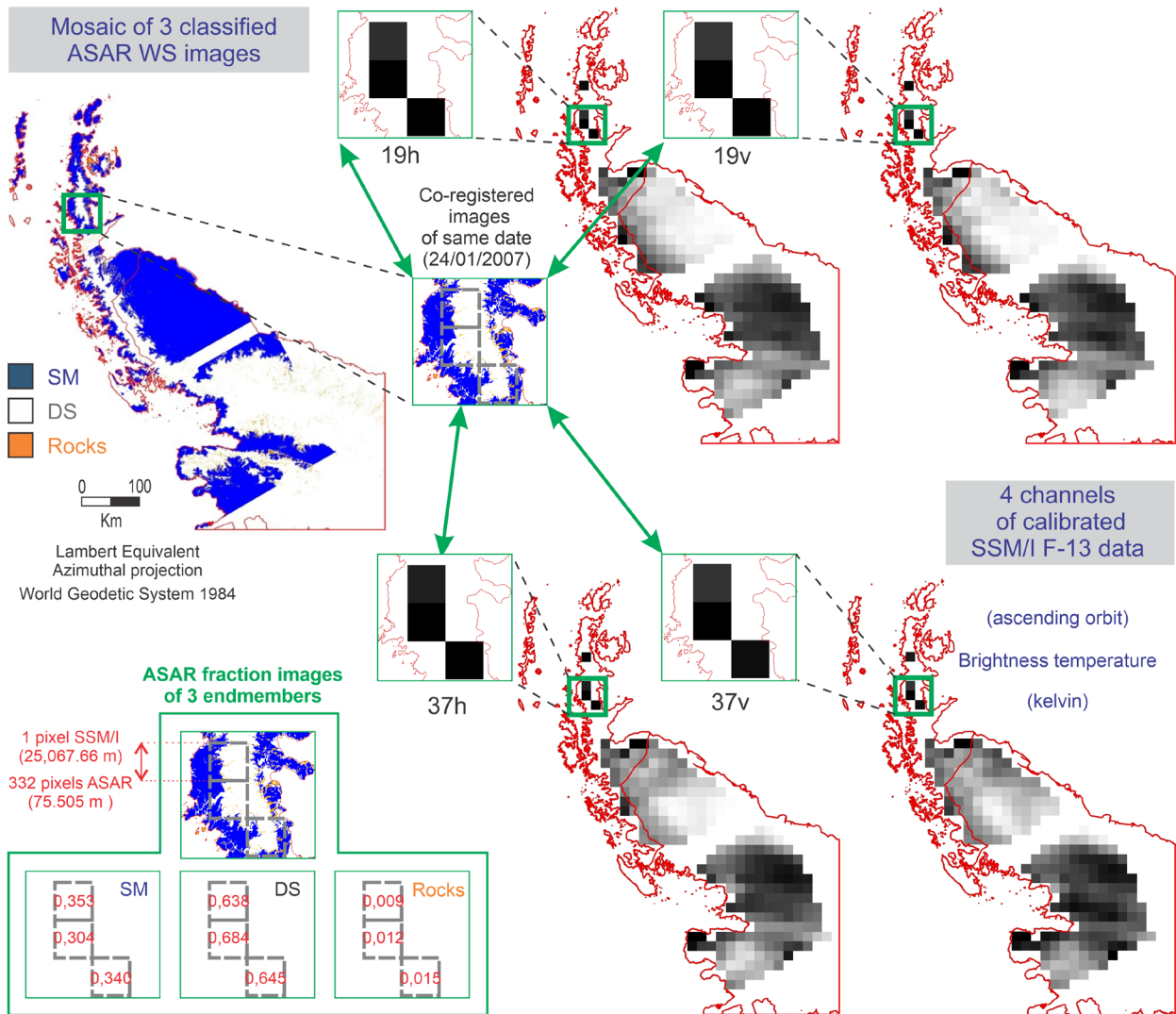


Figure 2. Classified ASAR images of snowmelt, dry snow, and rock outcrops, and correspondent calibrated SSM/I images in four channels (24/01/2007), covering the Antarctic Peninsula, used in the SLMM to estimate the spectral signatures of these endmembers in the studies of Mendes Jr. (2010) and Freitas et al. (2018).

co-registered and from the same date, with a resampled spatial resolution of 25 km), were then used in the SLMM to estimate the spectral signature of these components, using the least squares solution determined by Haertel & Shimabukuro (2005), expressed as:

$$r_k = (F^T F)^{-1} F^T R_k \tag{Equation 3}$$

where F^T is the transposed $n \times m$ matrix of proportions of each endmember.

In the study of Freitas et al. (2018) were used 16 ASAR fraction images of endmembers and 16 registered SSM/I F13 images at the same acquisition period (2006–2008) in the SLMM to estimate the unknown spectral signatures (Equation 3). The coefficient of determination (R^2) was higher than 0.98 and p-values lower than 0.00001 for all channels.

The estimated spectral signature of each pure component by Equation 3 and the corresponding SSM/I channels were then used

in the SLMM to estimate the image fraction of each component, through Equation 2.

Mendes Jr. (2010) applied the spectral signatures of pure components calculated in his study to estimate snowmelt image fractions in a 30-year time series of daily calibrated SMMR and SSM/I images, covering the Antarctic Peninsula (1978-2008). To assess the accuracy of the snowmelt fraction images, this author used an independent dataset and compared the estimated summer fraction images of snowmelt with ASAR fraction images, and found an average overall accuracy of 73% for images with class ranges of 0.2 (i.e., each class represents 20% of one pixel).

Freitas et al. (2018) used their spectral signatures and SSM/I images to estimate snowmelt fraction images for the Antarctic Peninsula in a shorter period (1999-2009) than Mendes Jr. (2010). The estimated summer fraction images of snowmelt were compared with fraction images with an independent ASAR classified image dataset of 11 dates (608 values, from 2006 to 2008). The Root Mean Squared Error (RMSE) of the estimated snowmelt fraction images was lower than 0.06 for all dates, except for one with 0.29, pointing to low errors in general.

The subpixel analysis approach using passive microwave sensors has been successfully applied in other studies and has opened up new research possibilities. Lemos et al. (2019) applied this approach to estimate areas of surface melting on the Wilkins Ice Shelf in the West Antarctic Peninsula. They also established relationships between the persistence of snow surface melting and the events of ice shelf break-up and disintegration that occurred on this ice shelf.

Hillebrand et al. (2022) used this SLMM in passive microwave radiometer data for sea ice mapping in the northwest of the Antarctic Peninsula. This region comprises the

endmembers Open Water and/or New Ice, and the Young and/or First Year Ice. The validation of the fraction images estimated for these two endmembers was carried out by comparing them with an independent dataset of sea ice concentration derived from 30 classified images from Sentinel 1A. Low errors were found for these estimated fraction images: a mean difference of 1.4%, with a standard deviation of 13.6%, and an RMSE of 15.3% in comparison to the ice concentration derived from Sentinel 1A.

MATERIALS AND METHODS

The procedures applied in this study can be divided into three main steps: selection of images (according to specific channels and polarization mode, type of orbit, and type of product available), pre-processing (comprising radiometric calibration, processing of noise or missing data, and masking images), and the subpixel analysis of snowmelt in passive microwave images, covering the Antarctic continent. To enhance clarity, we have provided a flowchart in Figure 3 to outline our processing chain for estimating snowmelt areas from passive microwave imagery.

We used SMMR, SSM/I, and SSM/IS data processed into Equal-Area Scalable Earth (EASE)-Grid brightness temperature, which are products available at the National Snow and Ice Data Center - NSIDC (<https://nsidc.org/data/nsidc-0630/versions/1>). These are a Level-3 EASE-Grid 2.0 Brightness Temperature dataset (code NSIDC-0630), collected since 25 October 1978, and are part of the NASA Making Earth System Data Records for Use in Research Environments (MEaSUREs) program. Table 1 shows the temporal coverage by sensor and platform for NSIDC-0630.

The southern hemisphere products have a spatial resolution of 25 km for the 18/19 GHz

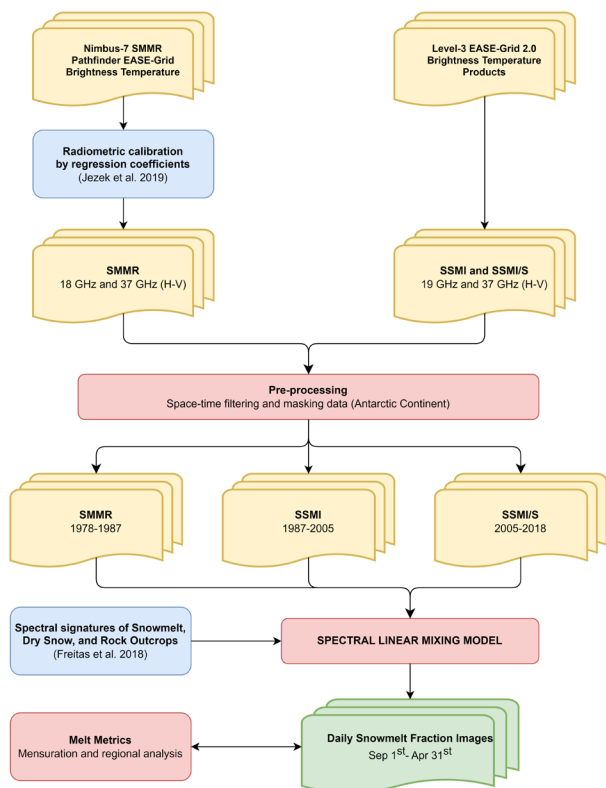


Figure 3. Methodological approach used in this study for estimating snowmelt areas from passive microwave imagery.

and 37 GHz channels (both horizontal e vertical polarization) and fully cover the Antarctic continent and the surrounding Austral Ocean. These EASE-Grid images are in the Lambert equivalent azimuthal projection and data referenced to the World Geodetic System 1984 (WGS84). The original values of brightness temperatures were preserved in data resampling and their radiometric accuracy is 0.1 K (Poe 1990, Galantowicz & England 1991). We chose EASE-Grid data from these channels and frequencies, acquired during descending orbits of SSM/I F8 and ascending orbits for the other sensors/ platforms because these observations of Earth’s surface occur closer to the strongest melt period of the day (Liu et al. 2006).

SSM/I F8 dataset comprise September 1987 to December 1991, but this radiometer did not acquire images during 28 days in December

1987 (Knowles et al. 2002, Armstrong et al. 2003). Brodzik et al. (2016) reported that brightness temperature values from the SSM/IS F17 37V channel have all 0 K or Not Available Number (NaN) data since April 2016. These inconsistent values could not be computed because the data were missing or flagged as too low quality in the input file. During our study, a noteworthy data gap of more than 10 consecutive days was observed for all SSM/IS instruments in both 2018 and 2019. Furthermore, the data for SSM/IS F17 and F18 was missing for the majority of January 2022. Due to these limitations, we had to rely on SSM/IS F16 data for our analysis. As a result, the time series analysis conducted in our study spanned from 1978 to 2018, excluding the period of 1987-1988.

SSM/I and SMM/IS images are cross-calibrated in the Level-3 EASE-Grid 2.0 Brightness Temperature dataset, except for SMMR images (Brodzik et al. 2016). Thus the regression coefficients calculated by Jezek et al. (1993) were used in this research to calibrate the brightness temperature values of SMMR images in the 18 GHz and 37 GHz channels (for both horizontal and vertical polarizations).

The preprocessing of SSMR, SSM/I, and SMM/IS images was based on the procedures proposed by Freitas et al. (2018). To eliminate erroneous data caused by noise or missing data, we interpolated missing image values by taking the average of the previous and subsequent imaged days. The same method was applied to interpolate bad data pixels using an iterative algorithm. First, bad pixels were interpolated using the average of the nearest two days with valid brightness temperature measures. Then, the remaining bad pixels were interpolated using the average of the nearest three days, followed by the nearest four days, and so on, up to a maximum of six days. After that, we sampled pixels located only in the continental

Table I. Temporal Coverage of the SMMR, SSM/I and SSM/IS sensors.

Sensor	Platform	Begin Coverage	End Coverage
SMMR	Nimbus 7	25 October 1978	20 August 1987
SSM/I	F08 F10 F11 F13 F14 F15	September 1987 December 1990 03 December 1991 03 May 1995 07 May 1997 23 February 2000	31 December 1991 14 November 1997 16 May 2000 19 November 2009 23 August 2008 09 August 2021
SSM/IS	F16 F17 F18 F19	01 November 2005 01 March 2008 08 March 2010 27 November 2014	Present Present Present 09 February 2016

area, by using the newest high-resolution vector polylines of the Antarctic coastline provided by the Antarctic Digital Database – ADD (Gerrish et al. 2022).

A subpixel mixture analysis was conducted to generate the time series of snowmelt fraction images for the Antarctic continent from 1978 to 2018. This involved using calibrated microwave brightness temperature images for channels 18/19H, 18/19V, 37H, and 37V in Equation 2, as well as spectral signatures of endmembers snowmelt, dry snow, and rock outcrops that were previously calculated by Freitas et al. (2018). The spectral signature of these endmembers in each channel and polarization mode is described in Table II.

The fraction images were used for the calculation of the snowmelt average areas during the period 1978-2018. The results were grouped from September 1st to April 31st since it comprises all the typical seasonal snowmelt cycles in Antarctica (Liu et al. 2006, Mendes Jr. 2010).

The daily fraction images were used to calculate the extension, intensity, frequency, and duration of the superficial snowmelt for seven different regions: the Antarctic Peninsula, Mary Bird Land, Ross Ice Shelf, Wilkes Land, Dronning

Maud Land, Amery Ice Shelf, and Filchner-Ronne Ice Shelf. These regions were delimited to enable comparisons between the results obtained in this research and the studies of Liu et al. (2006) and Trusel et al. (2012).

To determine the overall extent of snowmelt in Antarctica, we performed a calculation by multiplying the pixel area (625 km²) with the cumulative sum of all pixel values encompassing this continent. To mask unwanted values and calculate the total area for the aforementioned regions of Antarctica, we utilized georeferenced vector polylines. Since most snowmelt areas occur in December, January, and February, and have low values in the other months analyzed (Liu et al. 2006), we only used the fraction images of austral summer for calculating the total and median area of snowmelt for 1978-2018, and to the analysis of interannual variation of snowmelt in this period.

In this study, the concept of the total area of snowmelt refers to the daily accumulation of snowmelt during the summer season. It represents the combined surface area where the snow has melted over a given day, serving as a measure of the extent, duration, and magnitude of snowmelt within that period.

Table II. Brightness temperatures (K) of the endmembers Snowmelt, Dry snow and Rock outcrops

Endmember / Channel	19H	19V	37H	37V
Snowmelt	256.122	269.679	239.865	251.192
Dry snow	200.256	227.464	204.568	224.161
Rock outcrops	261.514	287.697	215.217	227.824
R^2	0.99	0.98	0.98	0.98

All models were significant (p-value < 0.0001).

The decision to utilize the median estimator for calculating the intensity of snowmelt, as opposed to a mean calculation, was made due to the presence of low values that typically occur at the start and end of the ablation season. These low values have the potential to disproportionately affect the overall estimations if a mean calculation were employed. Following the recommendation of Liu et al. (2006), we adopted the use of the median estimator as it has been observed to be a more robust and representative measure of snowmelt intensity.

Using the Mann-Kendall test, we performed a trend analysis for the annual estimations of the total and median area of snowmelt. We also used this dataset from austral summers to map the intensity of snowmelt, through the calculation of median values of fraction images. To map the persistence of snowmelt in Antarctica, we calculated the median number of days when each pixel value was higher than 0.8 (i.e., snowmelt greater than 80%) during the austral summers of this period.

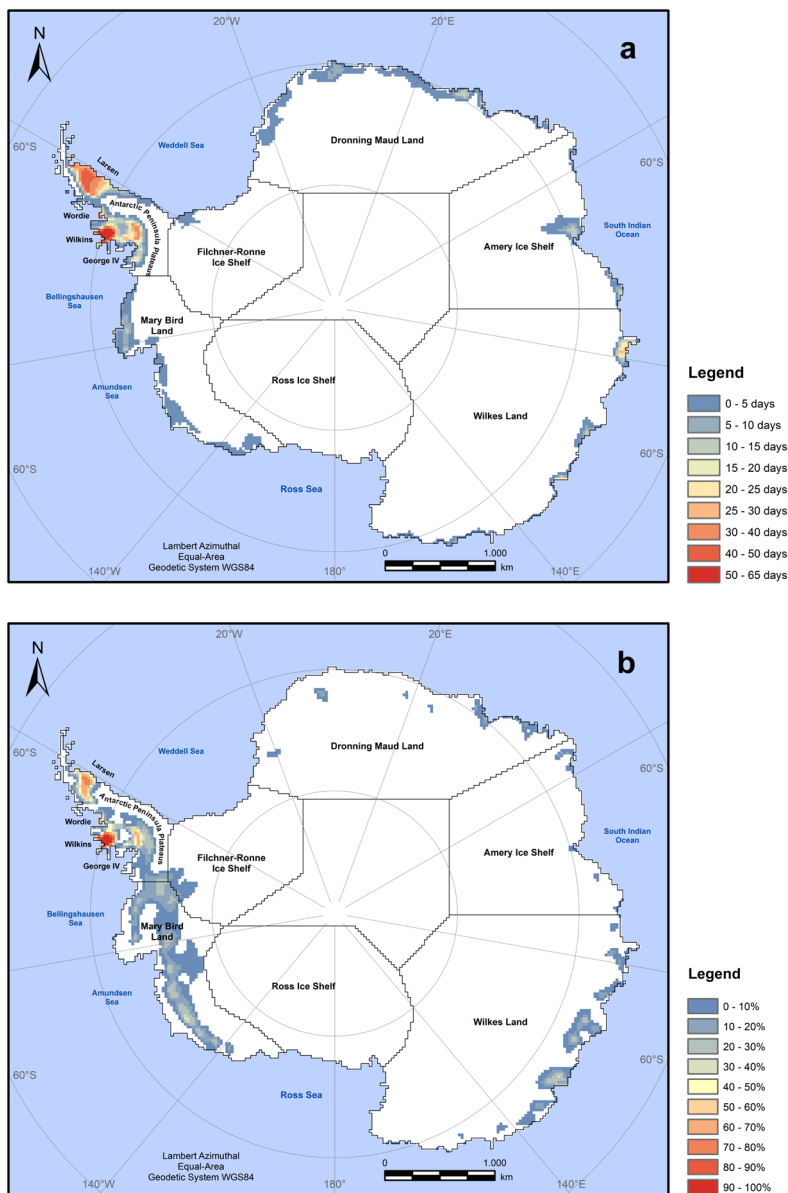
RESULTS AND DISCUSSION

The daily fraction images estimated by the SLMM were used to calculate the frequency and intensity of superficial snowmelt for different regions of the Antarctic continent, and this information was compiled in the maps of Figure 4. The total and median area of snowmelt and

its linear trend for Antarctica and all these regions are shown in the graphs of Figure 5.

Liu et al. (2006) and Trusel et al. (2012) observed that snowmelt areas usually expand from coastline to interior, from lower to higher latitudes and altitudes, and contract in the opposite direction, mainly because the surface air temperatures increase and decrease following this pattern, as the summer season progresses. Therefore, the snowmelt extension has an inverse relationship with increasing latitude, altitude, and continentality, which contribute to the reduction of surface air temperatures. These temperatures can become insufficient to melt the superficial snowpack in some parts of the Antarctic Peninsula, such as in high-altitude areas in the plateaus that divides this peninsula into western and eastern regions. As expected, none of the pixels in these plateaus exhibited a fraction value greater than 0.8 in our study (Figure 4a). Moreover, the median values remained consistently at zero throughout the austral summers spanning from 1978 to 2018 (Figure 4b).

The spatiotemporal analysis of the estimated snowmelt fraction images indicated that the most persistent and intensive melt in austral summer was observed on the Antarctic Peninsula (Figures 4a and 4b, respectively). Other main regions with persistent and intensive melt were Mary Bird Land and Wilkes Land, followed by Dronning Maud Land, Amery



Ice Shelf, Filchner-Ronne Ice Shelf, and Ross Ice Shelf (Figures 4 and 5).

The snowmelt average areas during the austral summers of 1978-2004 for the Antarctic Peninsula were also calculated and are graphically represented in Figure 6, to compare these values with the same period of melt extent data of the Antarctic Peninsula quantified by Liu et al. (2006).

The variation of the average total area of snowmelt during 1978-2004 approximates

a normal distribution in both studies, with differences in amplitude, mean, and standard deviation. The total area of snowmelt in the Antarctic Peninsula quantified in this study and by Liu et al. (2006) was less representative in September, October, and March (Figure 6), which are months characterized by a higher frequency of days with negative surface air temperatures than November to February.

The Antarctic Peninsula stands out as the initial region to witness melting areas and the

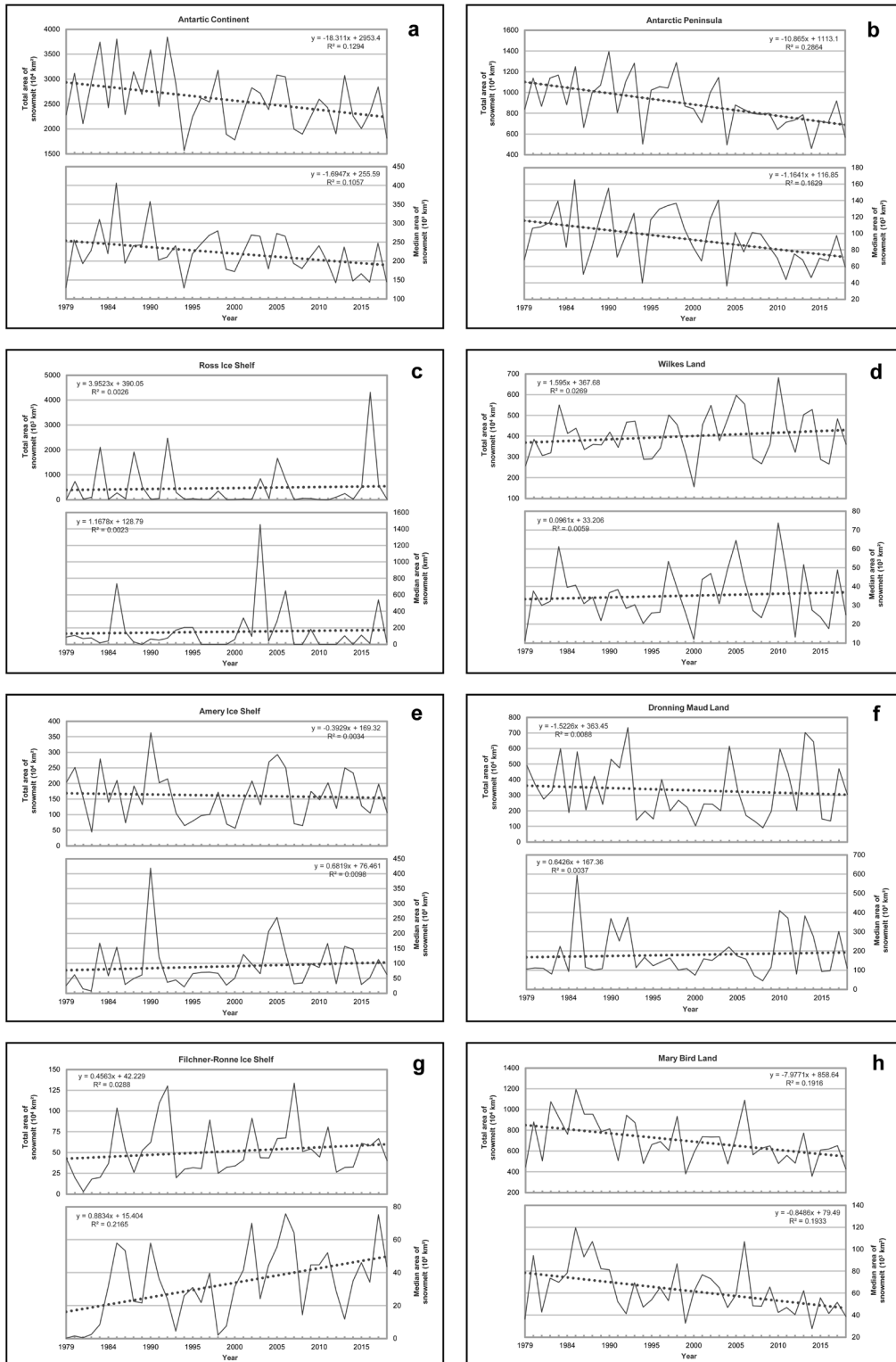


Figure 5. Total area and median area of snowmelt in Antarctica (a) and for all regions of this continent in austral summers of 1978-2018: the Antarctic Peninsula (b); Mary Bird Land (c); Ross Ice Shelf (d); Wilkes Land (e); Amery Ice Shelf (f); Dronning Maud Land (g); and Filchner-Ronne Ice Shelf (h). The linear trend of each time series is represented by a red dashed line. The equations and coefficient of determination (R^2) of each linear trend are described above the graph.

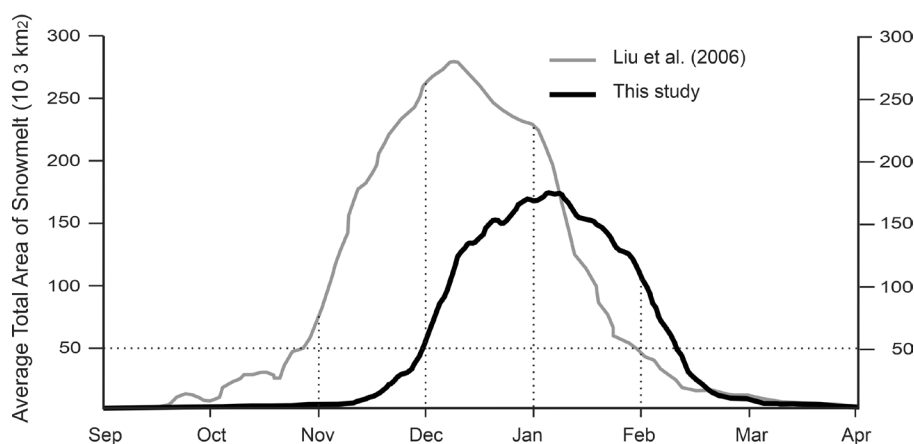


Figure 6. Average total area of snowmelt on the Antarctic Peninsula from September to April, for the period 1978-2008, calculated in this study and by Liu et al. (2006).

last to undergo refreezing in Antarctica. Liu et al. (2006) showed that the average total area of snowmelt in the Antarctic Peninsula exceeded 50,000 km², which accounts for approximately 9% of the peninsula's overall area, starting from late October. The extent of snowmelt reached its highest peak during the second week of December, gradually declining thereafter until early February when it became smaller than the initial measurement. Similarly, our study unveiled that the average total area of snowmelt also commenced in late October, surpassing the aforementioned threshold in early December. On January 7th, the peak extent of snowmelt was recorded at 177,274.49 km² (Figure 6). Subsequently, the area began to diminish and by mid-February, it returned to a value smaller than the peak measurement. Both studies found a similar onset date for the melt season, which closely aligns with the findings reported by Barrand et al. (2013). Using high-resolution scatterometer data (2.225km) from QuikSCAT, Barrand et al. (2013) revealed that the melt season in the Antarctic Peninsula typically begins in early November. They identified the South Shetland Islands, northern Antarctic Peninsula, and Wilkins ice shelf as the initial regions to experience snowmelt. Remarkably, these same two regions were also identified as the first areas to undergo snowmelt in Antarctica in this study.

According to data from the median number of days with snowmelt greater than 80% (Figure 4a) and median percentual area of snowmelt (Figure 4b), the areas with the highest snowmelt in Antarctica remained the same in 1978-2018: Larsen, Wilkins, George VI ice shelves (northeast region) and Wordie Ice Shelf (west region). We observed that the median duration of melting in the Antarctic Peninsula from 1978 to 2018 (Figure 4a) closely aligned with the findings of Liu et al. (2006) for 1978-2004 (median duration of 59.6 ± 5.4 days).

Trusel et al. (2012) utilized images from the SeaWinds scatterometer (spatial resolution of 4.45 km) aboard the QuikSCAT satellite to investigate the variability in Antarctic surface melting from 1999 to 2009. Their study highlighted that the Antarctic Peninsula had the longest melt seasons compared to the other regions analyzed. Specifically, portions of the Wilkins, Larsen C, and George IV ice shelves, as well as outlet glaciers along the western Antarctic Peninsula, exhibited an average melt duration exceeding 100 days per year. It is worth noting that our research yielded lower results for these regions in terms of median melt duration (Figure 4a), but this disparity was a result of using an 80% threshold to calculate the number of days with snowmelt during summers. If we had employed a lower threshold, it is highly likely

that we would have obtained significantly higher average melt durations per year.

Our trend analysis of total area of snowmelt found negative values for the entire Antarctic continent (Figure 5a) and the Antarctic Peninsula (5b), Marie Byrd Land (5h), Amery Ice Shelf (5e), and Dronning Maud Land (5f) regions. On the other hand, positive trends of total area of snowmelt were observed in the Ross Ice Shelf (5c), Filchner-Ronne Ice Shelf (5g) and Wilkes Land (5d). Taking into consideration these results, we can distinguish two different snow-melting trends according to two groups of regions in the Antarctic continent, which showed a negative trend as a whole.

The negative interannual trend of the total area of snowmelt on the Antarctic Peninsula was also observed by Zwally & Fiegles (1994) in nine years of SMMR data and by Torinesi et al. (2003) in eighteen years of SMMR and SSM/I data. Torinesi et al. (2003) conducted a study on the Antarctic cumulative melting surface and found a notable decrease of $1.8\% \pm 1\%$ per year between 1979 and 1999. This finding agrees with the discovery of a mean January cooling of the continent through infrared satellite data, as reported by Comiso (2000). These authors also noted that the cumulative melting surface of the peninsula primarily relies on the duration of melting rather than its variability, which tends to be low. In contrast, the larger ice shelves experience brief periods of melting, but their melting surface exhibits significant variability.

Liu et al. (2006) conducted an extensive observation of various regions in Antarctica, including the Antarctic Peninsula, the Amery Ice Shelf, Queen Maud Land, Marie Byrd Land, and the Ross Ice Shelf. Their study revealed a consistent negative interannual trend in both Melt Extent and Melt Index across these regions during the period from 1979 to 2004. On the other hand, Filchner-Ronne Ice Shelf had a slightly

positive trend in snowmelt areas. According to Liu et al. (2006), this is the region of Antarctica that has the shortest melt season, mainly in late December and January, and it was the only region that had a positive trend in both Melt Index ($0.0041 t + 0.7875$) and Melt Extent ($180.56 t + 93,740$) during the period 1978-2004.

The Melt Extent is calculated by multiplying each pixel where melting occurred on at least one day in the summer (Liu et al. 2006, Trusel et al. 2012). The concept of the Melt Index was introduced by Zwally & Fiegles (1994), and it was used to measure the total amount of melting, defined by the product of the total area of pixels that showed at least one day of melting in the snowpack by the number of days of melting that occurred over a year. As the Melt Index (measured in $\text{days} \cdot \text{km}^2$) takes into account the extent and duration of the snowmelt, it provides a more complete estimate of the amount of melting in a region than the total area of snowmelt.

Ross Ice Shelf and Wilkes Land were reported by Liu et al. (2006) as being the following regions with the shortest melt season and low average area of melt in Antarctica. They observed a slight decrease in Melt Index ($-0.0085 t + 2.7492$) and a positive trend in Melt Extent ($271.69 t + 114,061$). However, Liu et al. (2006) mentioned these linear trends from the regression analysis were found to be statistically insignificant due to the low correlation coefficient. During a more recent timeframe spanning from 1999 to 2009, Trusel et al. (2012) conducted a study that yielded findings consistent with those observed by Liu et al. (2006). Specifically, their research indicated that the Antarctic Peninsula and Filchner-Ronne regions displayed notable distinctions compared to other areas within Antarctica, exhibiting an almost inverse response to interannual variations.

The negative trend of snowmelt areas in Antarctica could also be attributed to the

disintegration or break-up of extensive ice shelves in these regions from 1978-2018. Scambos et al. (2000) demonstrated that the ice-shelf breakup has increased in Antarctica, and this process is preceded by an intense ponding of meltwater at the surface of these ice shelves. Therefore, these ice masses were located in coastal areas and experienced high and persistent snowmelt throughout this period. The decrease of these ice shelves likely contributed to the reduction in snowmelt areas and the overall negative trend observed. Cook & Vaughan (2010) used a time series of ice front changes around the Antarctic Peninsula from 1940 to 2002, and a coastal-change dataset updated using Envisat ASAR images from 2008/9, and observed an ice shelf loss of 18% (about 28,000 km²).

The interannual variations of the total area of snowmelt in the Antarctic Peninsula during the 1978-2004 period were also different in our study and Liu et al. (2006). These differences can be explained by the method used to quantify the total areas of snowmelt. Liu et al. (2006) calculated the total areas of each seasonal cycle of snowmelt in the Antarctic Peninsula by adding the areas of all pixels that had at least one day of snowmelt during the year. Thus, when a snowmelt event was detected by the abrupt transition of brightness temperature values in the analyzed time series, the pixel area of the SMMR or SSM/I images was added to the areas of other pixels that met this condition. In this study, this total area was calculated by multiplying the pixel area with the cumulative sum of all pixel values of snowmelt fraction images from austral summer.

In the study of Liu et al. (2006), the entire area covered by each pixel in the SMMR or SSM/I images (625 km²) was considered snowmelt, from the first to the last abrupt transition of brightness temperature, in a single channel of these sensors (19H), whereas in this study the

area of snowmelt was estimated at a subpixel level (i.e., values of the fraction images), based on the use of four channels of these images and the spectral signature of endmembers in the SLMM.

The discrepancy in snowmelt area estimates could also be explained by the use of different coastline polylines for extracting continental data from the SMMR and SSM/I images. Liu et al. (2006) utilized an Antarctic coastline derived from the RADARSAT 1 mosaic of 1997 (Liu & Jezek 2004), while this study employed the 2022 coastline from the ADD (Gerrish et al. 2022). Cook & Vaughan (2010) reported the Antarctic Peninsula's coastline underwent regression from 1978 to 1997, particularly on the ice shelves that exhibited a high frequency and intensity of snowmelt areas during the austral summer. This regression was another contributing factor to the disparities observed in the total quantified snowmelt areas between these studies. Subsequent significant variations in the coastline of the Antarctic Peninsula occurred after 1997, as documented in historical data from the ADD (Gerrish et al. 2022), further contributing to the differences in results reported by Liu et al. (2006).

For the comparison of the total areas of snowmelt in the austral summers of 1978-2004, quantified in this study and by Liu et al. (2006), we calculated the median total area, median absolute deviation, coefficient of variation, linear trend, and annual variation for the Antarctic Peninsula during this period (Table III).

The median total area of snowmelt quantified by Liu et al. (2006) was 315.625 km², and in this study was equal to 105.098.9 km², about 33,3% lower. Similar median absolute deviation values were obtained in both studies (24.7 and 30.5 km², respectively), indicating some likelihood in the behavior of interannual variations of snowmelt total area (Table III).

Table III. Comparison of snowmelt area calculations for the Antarctic Peninsula (1978-2004) between Liu et al. (2006) and current study.

Statistic	Liu et al. (2006)	This study
Median total area of wet snow (km ²)	315,625	105,098.9
Median Absolute Deviation	24,688	30,457.3
Coefficient of variation	0.0782	0.2898
Linear trend of wet snow	-1,137.2 t + 330,496	162.08 t + 91,783
Correlation coefficient	0.303	0.0008
Annual variation of wet snow area (km ²)	- 1,091.712	155.597

Liu et al. (2006) reported an annual decrease of 1,091.7 km² in the total area of snowmelt on the Antarctic Peninsula, while in this study was observed a slight annual increase of only 155.6 km² (Table III). A positive trend in the melting duration on ice shelves on the Antarctic Peninsula during the period 1978-1991 was observed by Ridley (1993), with a confidence level of 85%, through the analysis of SMMR and SSM/I images.

The seasonal variations of the estimated total areas of snowmelt in this study and by Liu et al. (2006) were more similar from 1990-2004. This can be explained by the greater availability of SSM/I images during this period compared to SMMR images. Thus, a closer approximation was observed between the total areas quantified in these studies. The behavior of snowmelt variations in 1990-2004 in this study (Figure 5b) was more similar to that of the Melt Index than to that of the total areas quantified by Liu et al. (2006).

Trusel et al. (2012) discovered that the maximum Melt Index and Melt Intensity in Antarctica occurred in 2005, while the minimum values were observed in 2000, during the period 1999-2009. These findings were supported by the QuikSCAT-derived melt fluxes, which were in agreement with the results obtained from the regional climate model RACMO2.1 and independent ground-based observations

(Trusel et al. 2013). It's worth noting that there are some differences in the melt metrics used in this study compared to the ones employed by Trusel et al. (2012). While Trusel et al. (2012) used the Melt Index, which considers the total annual melt duration and incorporates both spatial and temporal dimensions of melting in an entire area of a given pixel, the current study utilized the total and median area of snowmelt as melt metrics. Additionally, Trusel et al. (2012) calculated the Melt Intensity by summing all pixels experiencing melt for each day in the QuikSCAT dataset during the austral summer melt season. In contrast, the current study employed the median area of snowmelt fraction values as a measure of the magnitude of snowmelt. Despite these differences, the melt metrics of the total and median area of snowmelt in the current study exhibited maximum and minimum values in 2005 and 2000, respectively, from 1999 to 2009 (Figure 5b), aligning with the findings of Trusel et al. (2012, 2013).

Freitas et al. (2018) also utilized the same SLMM approach as our study to detect snowmelt in the Antarctic Peninsula, using QuikSCAT imagery with a resolution of 2.225 km. In their research, they successfully obtained precise estimations of snowmelt fraction images (RMSE < 0.09). These authors found that the temporal dynamics of the Melt Extent and Melt Index exhibited a more accurate pattern compared to

the conventional melt metrics obtained through Boolean snowmelt detection approaches (i.e., presence-absence of snowmelt) employed by Liu et al. (2006) and Trusel et al. (2012) for passive microwave sensors and scatterometer datasets, respectively. These Boolean approaches assumed that the entire detected pixel area indicated snowmelt, whereas in reality, snowmelt occurs within pixel fractions. Through a comprehensive multiscale analysis, the aforementioned study further supported the notion that melt metrics derived from Boolean approaches have a tendency to overestimate the true extent of snowmelt. This finding is in line with our own results, particularly when comparing the average area of snowmelt in the Antarctic Peninsula with findings of Liu et al. (2008) (Figure 6).

CONCLUSIONS

The analysis of melt metrics in passive microwave images indicates an overestimation that can be attributed to a decrease in spatial resolution resulting from a multiplicative effect of larger pixel areas. In other words, the traditional Boolean method of calculating melt metrics may lead to an overestimation of snowmelting since it assumes the entire area of a detected pixel is experiencing melting. This is because snowmelting occurs at pixel fractions. Thus, a sensitivity approach is needed to detect snowmelt areas in passive microwave imagery.

The estimated subpixel snowmelt fraction images covered a daily time series from 1978 to 2018, from September to April. Therefore, this study updated the results of previous investigations with an extended period of SSM/IS data and provided a subpixel snowmelt database on a temporal scale that did not previously exist. This comprehensive timeframe allowed us to examine a total of 39 snowmelt

cycles in Antarctica, providing valuable insights into the patterns and trends of snowmelt over the years.

The analysis of the estimated snowmelt fraction images revealed that the Antarctic Peninsula exhibited the highest levels of persistent and intensive melt, particularly pronounced on the Larsen, Wilkins, George VI, and Wordie ice shelves. The melting season in the Antarctic Peninsula typically began in late October, reached its peak in early January, and ended in late March. Additionally, significant snowmelt was observed in other regions such as Mary Bird Land and Wilkes Land, followed by Dronning Maud Land, Amery Ice Shelf, Filchner-Ronne Ice Shelf, and Ross Ice Shelf.

The trend analysis revealed contrasting patterns in snowmelting trends across different regions of the Antarctic continent. Negative trends were observed in the Antarctic Peninsula, Marie Byrd Land, Amery Ice Shelf, Ross Ice Shelf/Siple Coast, and Dronning Maud Land regions. In contrast, positive trends were identified in the Filchner-Ronne Ice Shelf and Wilkes Land regions. These findings indicate the presence of two distinct groups of regions with divergent snow-melting trends within the Antarctic continent. Overall, the Antarctic continent as a whole exhibited a negative trend in snowmelting.

To verify the accuracy of the estimated snowmelt fraction images by the SLMM in periods before or after the analysis in this study is recommended the use of classified images (or the classification of) medium and high spatial resolution of optical and RADAR images as reference data for snowmelt areas.

The estimated snowmelt fraction images from this study offer a valuable tool for accurately determining the duration of melting, enabling more precise calculations of the Melting Index during the austral summers spanning the period from 1978 to 2018. Furthermore, these images

can be utilized in models to predict surface water runoff resulting from snowmelt.

Due to the ongoing debate on global climate change and the instability of Antarctic ice shelves, continuous monitoring of snowmelt areas is of great importance in evaluating the magnitude and location of melting areas on a long-term temporal scale, as well as their impacts on glacial systems, local coastal environments, and sea-level rise.

Acknowledgments

To the National Snow and Ice Data Center (NSIDC), for making available all time series of SMMR, SSM/I, and SSMIS data in its Distributed Active Archive Center (DAAC).

REFERENCES

ABDALATI W, STEFFEN K, OTTO C & JEZEK KC. 1995. Comparison of brightness temperatures from SSMI instruments on the DMSP F8 and F11 satellites for Antarctica and the Greenland ice sheet. *Int J Remote Sens* 7: 1223-1229.

ABDALATI W & STEFFEN K. 1997. Snowmelt on the Greenland ice sheet as derived from passive microwave satellite data. *J Clim* 1: 3165-3175.

ADAMS JB, SMITH MO & JOHNSON PE. 1986. Spectral mixture modeling: a new analysis of rock and soil types at the Viking Lander 1 site. *J Geophys Res* 91: 8098-8112.

ARMSTRONG RL, KNOWLES KW, BRODZIK MJ & HARDMAN MA. 2003. DMSP SSM/I Pathfinder Daily EASE-Grid brightness temperatures. Boulder: National Snow and Ice Data Center (CD-ROM).

BARRAND NE, VAUGHAN DG, STEINER N, TEDESCO M, KUIPERS MUNNEKE P, VAN DEN BROEKE MR & HOSKING JS. 2013. Trends in Antarctic Peninsula surface melting conditions from observations and regional climate modeling. *J Geophys Res* 118: 315-330.

BEVAN S, LUCKMAN A, HENDON H & WANG G. 2020. The 2020 Larsen C Ice Shelf surface melt is a 40-year record high. *TC* 14: 3551-3564.

BRODZIK MJ, LONG DG, HARDMAN MA, PAGET A & ARMSTRONG R. 2016. MEaSURES Calibrated Enhanced-Resolution Passive Microwave Daily EASE-Grid 2.0 Brightness Temperature ESDR, Version 1. Boulder: NASA National Snow and Ice Data Center.

COMISO JC. 2000. Variability and trends in Antarctic surface temperatures from in situ and satellite infrared measurements. *J Clim* 13: 1674-1696.

COOK AJ & VAUGHAN DG. 2010. Overview of areal changes of the ice shelves on the Antarctic Peninsula over the past 50 years. *TC* 4: 77-98.

FAHNESTOCK MA, ABDALATI W & SHUMAN CA. 2002. Long melt seasons on ice shelves of the Antarctic Peninsula: an analysis using satellite-based microwave emission measurements. *Ann Glaciol* 34: 127-133.

FREITAS MWD, MENDES JÚNIOR C, ARIGONY-NETO J, COSTI J & SIMÕES J. 2018. A multiscale subpixel mixture analysis applied for melt detection using passive microwave and radar scatterometer image time series of the Antarctic Peninsula (1999-2009). *Ann Glaciol* 59: 16-28.

GALANTOWICZ JF & ENGLAND AW. 1991. The Michigan Earth Grid: Description, registration method for SSM/I data and derivative map projections. Michigan: University of Michigan Tech Rep Ann Arbor.

GERRISH L, FRETWELL P & COOPER P. 2022. High-resolution vector polylines of the Antarctic coastline. UK Polar Data Center, Natural Environment Research Council, UK Research & Innovation.

HAERTEL V & SHIMABUKURO YO. 2005. Spectral linear mixing model in low spatial resolution image data. *IEEE Trans Geosci Remote* 43: 2555-2562.

HILLEBRAND FL, BREMER UF, DE FREITAS MWD, COSTI J, MENDES JÚNIOR CW, ARIGONY-NETO J & SIMÕES JC. 2022. Spectral linear mixing model applied to data from passive microwave radiometers for sea ice mapping in the Antarctic Peninsula. *Geocarto Int* 37: 3141-3166.

JEZEK KC, MERRY C & CAVALIERI D. 1993. Comparison of SMMR and SSM/I passive microwave data collected over Antarctica. *Ann Glaciol* 17: 131-136.

KNOWLES KW, NJOKU E, ARMSTRONG RL & BRODZIK MJ. 2002. Nimbus-7 SMMR Pathfinder Daily EASE-Grid Brightness Temperatures. Boulder: National Snow and Ice Data Center (CD-ROM).

LEMOS A, ARIGONY-NETO J, MENDES-JÚNIOR CW & COSTI J. 2019. A comparative analysis between variations in wet snow zone and the main break-up and disintegration events in Wilkins ice shelf, Antarctic Peninsula. *Glob Planet Change* 177: 39-44.

LIU H & JEZEK KC. 2004. A complete high-resolution coastline of Antarctica extracted from orthorectified Radarsat SAR imagery. *PE&RS* 70: 605-616.

LIU H, WANG L & JEZEK KC. 2005. Wavelet-transform based edge detection approach to derivation of snowmelt onset, end and duration from satellite passive microwave measurements. *Int J Remote Sens* 26: 4639-4660.

LIU H, WANG L & JEZEK KC. 2006. Spatiotemporal variations of snowmelt in Antarctica derived from satellite scanning multichannel microwave radiometer and Special Sensor Microwave Imager data (1978-2004). *J Geophys Res* 111: 1-20.

MENDES JÚNIOR CW. 2010. Monitoramento da zona superficial de neve úmida da Península Antártica pelo uso de dados dos sensores SMMR e SSM/I - PhD thesis. Federal University of Rio Grande do Sul, Porto Alegre, RS, Brazil.

MENDES JÚNIOR CW, ARIGONY-NETO J, HILLEBRAND FL, FREITAS MWD, COSTI J & SIMÕES JC. 2022. Snowmelt retrieval algorithm for the Antarctic Peninsula using SAR imageries. *An Acad Bras Cienc* 94: e20210217. <https://doi.org/10.1590/0001-376520220210217>.

MOTE TL, ANDERSON MR, KUIVENEN KC & ROWE CM. 1993. Passive microwave-derived spatial and temporal variations of summer melt on Greenland ice sheet. *Ann Glaciol* 17: 233-238.

POE GA. 1990. Optimum interpolation of Imaging Microwave Radiometer Data. *IEEE Trans Geosci Remote* 5: 800-810.

RIDLEY J. 1993. Surface melting on Antarctic Peninsula ice shelves detected by passive microwave sensors. *Geophys Res Lett* 23: 2639-2642.

SCAMBOS TA, HULBE C, FAHNESTOCK M & BOHLANDERT J. 2000. The link between climate warming and break-up of ice shelves in the Antarctic Peninsula. *J Glaciol* 154: 516-530.

SHIMABUKURO YE. 1987. Shade images derived from linear mixing models of multispectral measurements of forested areas - Ph.D. thesis. Colorado State University, Colorado, USA.

SHIMABUKURO YE & SMITH JA. 1991. The least-squares mixing models to generate fraction images derived from remote sensing multispectral data. *IEEE Trans Geosci Remote* 29: 16-20.

TORINESI O, FILY M & GENTHON C. 2003. Interannual variability and trend of the Antarctic Ice Sheet summer melting period from 20 years of spaceborne. *AAAR* 1: 147-152.

TRUSEL LD, FREY KE & DAS SB. 2012. Antarctic surface melting dynamics: Enhanced perspectives from radar scatterometer data. *J Geophys Res* 117: 1-15.

TRUSEL LD, FREY KE, DAS SB & MUNNEKE PK. 2013. Satellite-based estimates of Antarctic surface meltwater fluxes. *Geophys Res Lett* 40: 6148-6153.

ZWALLY HJ & FIEGLES S. 1994. Extent and duration of Antarctic surface melting. *J Glaciol* 136: 463-476.

How to cite

MENDES JÚNIOR CW, ARIGONY NETO J, HILLEBRAND FL, FREITAS MWD, COSTI J & SIMÕES JC. 2023. Spectral Linear Mixing Model application in passive microwave data to analyze Antarctic surface melting dynamics (1978-2018). *An Acad Bras Cienc* 95: e20230732. DOI 10.1590/0001-3765202320230732.

Manuscript received on July 3, 2023; accepted for publication on November 10, 2023

CLAUDIO W. MENDES JÚNIOR¹

<https://orcid.org/0000-0003-1745-348X>

JORGE ARIGONY NETO²

<https://orcid.org/0000-0003-4848-2064>

FERNANDO L. HILLEBRAND³

<https://orcid.org/0000-0002-0182-8526>

MARCOS W.D. DE FREITAS⁴

<https://orcid.org/0000-0001-9879-2584>

JULIANA COSTI²

<https://orcid.org/0000-0001-6220-2343>

JEFFERSON C. SIMÕES⁴

<https://orcid.org/0000-0001-5555-3401>

¹Universidade Federal do Rio Grande do Sul (UFRGS), Departamento de Geodésia, Av. Bento Gonçalves, 9500, 91509-900 Porto Alegre, RS, Brazil

²Universidade Federal do Rio Grande (FURG), Instituto de Oceanografia, Avenida Itália s/n, Km 8, 96201-900 Rio Grande, RS, Brazil

³Instituto Federal de Educação, Ciência e Tecnologia do Rio Grande do Sul (IFRS), Rodovia RS-239, Km 68, 3505, 95700-000 Rolante, RS, Brazil

⁴Universidade Federal do Rio Grande do Sul (UFRGS), Departamento de Geografia, Av. Bento Gonçalves, 9500, 91501-970 Porto Alegre, RS, Brazil

Correspondence to: **Claudio Wilson Mendes Júnior**

E-mail: claudio.mendes@ufrgs.br

Author contributions

This manuscript was elaborated by Claudio Wilson Mendes Jr. and Jorge Arigony Neto, with pre-processing of passive microwave images and figure elaboration performed by Fernando Luis Hillebrand. Marcos Wellausen Dias de Freitas and Juliana Costi developed and implemented the Spectral Linear Mixel Model along with other scripts using Matlab. Jefferson Cardia Simões contributed to the review, editing, and discussion of the article's results.

